ADVANCED MATERIALS
www.advmat.de

In Situ Reconstruction of High-Entropy Heterostructure Catalysts for Stable Oxygen Evolution Electrocatalysis under Industrial Conditions

Jue Hu, Tianqi Guo, Xinyu Zhong, Jiong Li, Yunjie Mei, Chengxu Zhang, Yuebin Feng, Mingzi Sun, Lijian Meng, Zhiyuan Wang, Bolong Huang,* Libo Zhang,* and Zhongchang Wang**

Dedicated to the 70th Anniversary of Kunming University of Science and Technology

Despite of urgent needs for highly stable and efficient electrochemical water-splitting devices, it remains extremely challenging to acquire highly stable oxygen evolution reaction (OER) electrocatalysts under harsh industrial conditions. Here, a successful in situ synthesis of FeCoNiMnCr high-entropy alloy (HEA) and high-entropy oxide (HEO) heterocatalysts via a Cr-induced spontaneous reconstruction strategy is reported, and it is demonstrated that they deliver excellent ultrastable OER electrocatalytic performance with a low overpotential of 320 mV at 500 mA cm^{-2} and a negligible activity loss after maintaining at 100 mA cm^{-2} for 240 h. Remarkably, the heterocatalyst holds outstanding long-term stability under harsh industrial condition of 6 M KOH and 85 °C at a current density of as high as 500 mA cm^{-2} over 500 h. Density functional theory calculations reveal that the formation of the HEA-HEO heterostructure can provide electroactive sites possessing robust valence states to guarantee long-term stable OER process, leading to the enhancement of electroactivity. The findings of such highly stable OER heterocatalysts under industrial conditions offer a new perspective for designing and constructing efficient high-entropy electrocatalysts for practical industrial water splitting.

1. Introduction

The upcoming global energy and environmental crises are calling for the exploration of renewable energy, which is becoming increasingly urgent. Alkaline water electrolysis (AWE) for the mass production of hydrogen is considered as an advanced strategy.[1] However, the high overpotential of the anodic oxygen evolution reaction (OER) leads to sluggish kinetics, which jeopardizes the overall electrolytic efficiency. To date, despite that the overpotential of OER has been significantly lowered,[2] most of the electrocatalysts are only active under laboratory conditions at a low current density (e.g., 10 mA cm^{-2}). Their activity and stability at high current densities (e.g., ≈100–1000 mA cm^{-2}), which are crucial to industrial applications, are still scarcely explored.[3] Developing the OER catalysts with low-cost, industrially relevant

J. Hu, Y. Mei, C. Zhang, Z. Wang, L. Zhang
Faculty of Metallurgical and Energy Engineering
Kunming University of Science and Technology
Kunming 650093, China
E-mail: chxzhang@kust.edu.cn; lbzhang@kust.edu.cn

J. Hu, Y. Mei, Z. Wang, L. Zhang
Key Laboratory of Unconventional Metallurgy
Kunming University of Science and Technology
Kunming 650093, China

J. Hu, L. Zhang
Southwest United Graduate School
Kunming 650092, China

T. Guo, Z. Wang
International Iberian Nanotechnology Laboratory (INL)
Braga 4715-330, Portugal
E-mail: zhongchang.wang@inl.int

The ORCID identification number(s) for the author(s) of this article can be found under https://doi.org/10.1002/adma.202310918

DOI: 10.1002/adma.202310918

X. Zhong, J. Li
Shanghai Synchrotron Radiation Facility, Shanghai Advanced Research Institute
Chinese Academy of Sciences
Shanghai 201204, China

X. Zhong
University of Chinese Academy of Sciences
Beijing 100049, China

L. Meng
CIETI, ISEP, Polytechnic of Porto, Rua Sr. António Bernardino de Almeida
Porto 4249-015, Portugal

Y. Feng
Faculty of Science
Kunming University of Science and Technology
Kunming 650093, China

M. Sun, B. Huang
Department of Applied Biology and Chemical Technology
The Hong Kong Polytechnic University
Hung Hom, Kowloon, Hong Kong SAR China
E-mail: bhuang@polyu.edu.hk

activity and long-term durability is hence timely and ultimately important.

It is well known that metal sites normally show high affinity to the OER intermediates. However, the binding of the OER intermediates on the metal sites can be too strong, leading potentially to high energy barriers during the OER process.[4] Conversely, high-entropy alloys (HEAs) have attracted considerable attentions for the OER electrocatalysis owing to their positive multielemental synergy. Moreover, the structure of HEAs can be adjusted by controlling the compositions and ratios of the metal elements, which endows HEAs with enhanced OER properties.[5] For instance, Huo et al. reported that the introduction of Pd is responsible for the reduced energy barrier of the rate-determining step (RDS) of $O^*\rightarrow OOH^*$, resulting in high activity of the FeCoNiCuPd/CFC catalyst.[6] Moreover, Chen et al. found that the element segregation could lower the energy barrier of H_2O dissociation at the NiCoFeMoMn surface, leading to improved OER activity.[7] In addition, Wang et al. improved the electrocatalytic activity of HEAs by regulating the adsorption of reaction intermediates on metal sites.[4b] In our previous work, we reported that the strong adsorption of OH^* on the FeCoNi alloy for the OER process restrains the OER kinetics through further deprotonation of OH^*, and the introduction of Mo can attenuate the adsorption of OH^* on Fe, Co, and Ni sites, thereby accelerating the subsequent rate-determining deprotonation step and improving the OER performance of the FeCoNiMo HEA catalyst.[8] Although the binding energy distribution among the high-entropy compositions results in enhanced OER activity for HEAs, the HEA particles actually undergo catastrophic oxidation. Consequently, the metals aggregate on the outside layers, which are accompanied by the formation of disordered oxide shell on the HEA particles.[9] The random surface reconstruction can easily occur in the oxidized OER conditions, and as a result, the stabilization role of high-entropy compositions can hardly be fulfilled.[10] Additionally, achieving long-term tolerance of HEA catalysts under harsh OER industrial conditions still poses a significant challenge, especially when non-noble metals are adopted.

Here, we report the successful in situ reconstruction of non-noble high-entropy alloy and high-entropy oxide (HEA-HEO) FeCoNiMnCr heterostructures for highly stable oxygen evolution even under industrial conditions. As a result of such HEA-HEO heterostructures, the metal particles can be stabilized during the OER electrocatalysis by a strong interaction with HEO.[11] Furthermore, the strong binding of the oxygen-containing intermediates on the active metal sites is largely weakened due to the repulsive interaction with the oxide species on the neighboring HEO, thus improving the OER kinetics and simultaneously increasing stability of the HEA-HEO catalysts.[12] The HEA-HEO heterocatalyst is synthesized by an early transition metal induced in situ phase transition from the HEA, which stimulates abundant active HEA-HEO interfaces exposed on the surface of the catalyst to accelerate the OER process. In virtue of this unique strategy, the as-prepared FeCoNiMnCr HEA-HEO heterocatalyst shows an ultralow overpotential of 247 mV at 100 mA cm^{-2} after 100 h and an outstanding long-term stability with negligible activity loss after maintaining at 500 mA cm^{-2} for 500 h under harsh industrial conditions (6 M KOH and 85 °C). Density functional theory (DFT) calculations reveal that the HEO formation enhances electroactivity by breaking the strong 3d orbital overlapping effect, which uplifts the d-band center of active sites for the efficient and durable OER. This work offers inspiration to the design of HEA-based delicate heterostructure to realize both electroactivity and stability of catalysts for industrial applications.

2. Results

2.1. Synthesis and Structural Characterization

The FeCoNiMnCr HEA-HEO heterostructure was synthesized by in situ Cr-induced spontaneous reconstruction strategy (**Figure 1a**). As an early transition metal, Cr is often intrinsically reactive to form highly stable oxides owing to its electropositive and oxophilic nature. Such tendency can also be revealed in the Ellingham diagram, which illustrates oxidation potentials of different metals. As shown in Figure S1 (Supporting Information), Cr is close to the bottom of the Ellingham diagram, which indicates that it has high oxidation potentials and is prone to form oxide.[13] Therefore, the composition of the high-entropy products can be adjusted in terms of their metallic and oxide states by tuning reaction temperature and time through this Cr-induced synthesis strategy. In situ Raman spectroscopy (Figure 1b,c) shows the structure changes of the FeCoNiMn-MOF and FeCoNiMnCr-MOF precursors and the formation of the FeCoNiMn HEA/CNT and FeCoNiMnCr HEA-HEO/CNT during the pyrolysis process. The peaks at ≈578–603 cm^{-1} for the FeCoNiMn-MOF and FeCoNiMnCr-MOF correspond to the C—H stretching region of the benzene ring of MOFs.[2c] As shown in Figure 1c, when the calcination temperature is lower than 175 °C, the structure of MOF precursor does not change. When the temperature rises to 200 °C, new characteristic peaks appear at 554 and 671 cm^{-1}, while the characteristic peak at 603 cm^{-1} decreases and then vanishes. The newly formed peaks at 554 and 671 cm^{-1} during the synthesis of the FeCoNiMnCr HEA-HEO reflect the M—O vibrational mode,[14] which is not identified in the Cr-free FeCoNiMn HEA, demonstrating the successful application of in situ Cr-induced reconstruction strategy for synthesizing the FeCoNiMnCr HEA-HEO heterostructure.

X-ray diffraction (XRD) analysis reveals that there is no significant change in diffraction peak position of the precursors after the introduction of Cr (Figure S2, Supporting Information). The XRD patterns of the FeCoNiMn HEA/CNT are presented in Figure S3 (Supporting Information), which corresponds to a clear face-centered-cubic (FCC) structure with diffraction peaks of (111), (200), and (220) planes of the FeCoNiMn HEA/CNT. Especially, compared with the diffraction peaks of the Fe- and Ni-based alloys, the position of diffraction peaks of the FeCoNiMn HEA/CNT sample is shifted remarkably, indicating that elements are successfully introduced into the nanocatalysts to form the HEA structure. Based on the actual metal content, we further calculated the actual mixing entropy of FeCoNiMn HEA/CNT to be 1.38R (Table S1, Supporting Information), further verifying that the synthesized FeCoNiMn alloy is HEA.[15] The high-resolution TEM (HRTEM) (Figure S4, Supporting Information) image shows that lattice spacing of the alloy is 0.208 nm, which corresponds to the (111) facet of HEA crystals. Meanwhile, the FeCoNiMnCr HEA-HEO/CNT also has an FCC structure with a new metal oxide phase, which originates from the spontaneous formation of oxide states after the introduction of Cr (**Figure 2a**).

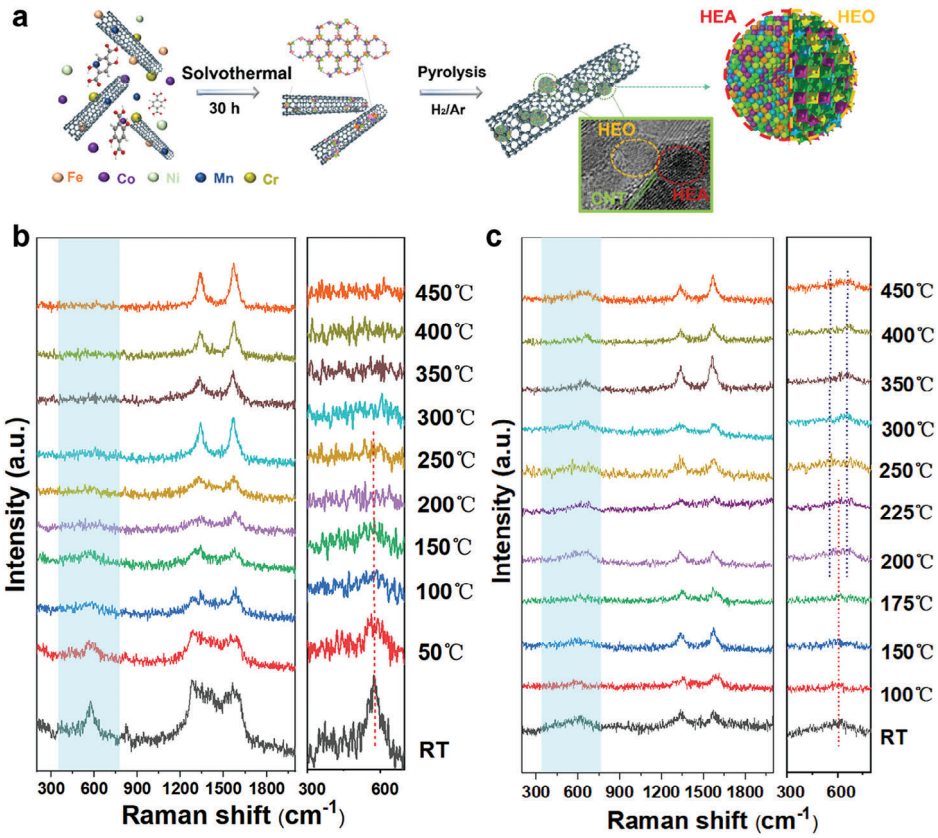

Figure 1. Synthesis process of the FeCoNiMnCr HEA-HEO/CNT catalyst. a) Schematic illustration of synthesis process of the FeCoNiMnCr HEA-HEO/CNT catalyst. In situ Raman characterization of b) the FeCoNiMn MOFs/CNT and c) FeCoNiMnCr MOFs/CNT precursor at different temperatures during the pyrolysis process.

The newly formed XRD peaks (pink line) of the FeCoNiMnCr HEA-HEO/CNT at ≈35° and ≈64° belong to (311) and (440) planes of the spinel oxide, respectively. All diffraction peaks of the FeCoNiMnCr HEA-HEO match well with the corresponding standard patterns of the spinel oxide $NiCrMnO_4$ (JPCDS 71-0854), further confirming the HEOs formation. No obvious characteristic peaks of organic substances are identified in the FT-IR spectra, indicating the absence of organic residues in the synthesized FeCoNiMnCr HEA-HEO/CNT and FeCoNiMn HEA/CNT catalysts (Figure S5, Supporting Information).

The morphologies of the FeCoNiMnCr HEA-HEO and the FeCoNiMn HEA are shown in Figure 2b; and Figure S6 (Supporting Information). The FeCoNiMnCr HEA-HEO nanoparticles are uniformly distributed on the CNT substrate (Figure 2c). From the HRTEM images (Figure 2d; and Figure S7, Supporting Information), one can clearly see that the carbon nanotubes with a lattice spacing of 0.338 nm for carbon (220) plane and the nanoparticles with a particle size of 4.18 ± 0.177 nm are anchored on the CNT carriers. The close contact of catalyst particles to the conductive CNT carriers can enhance electron transfer and reduce the loss of active sites during the reactions. The HEO and HEA particles can be clearly distinguished, which are connected to form heterogeneous interfaces. A single-phase FCC with a lattice spacing of 0.209 nm is formed in the HEA (Figure 2e), which is indexed to (111) facet of FCC. The lattice spacing of 0.253 nm in Figure 2f can be attributed to the (311) crystal plane of HEO. Further fast Fourier transformation (FFT) patterns reveal the presence of the (111) facet of HEA and (311) and (400) facets of HEO (Figure 2i and ii), suggesting a successful in situ construction of the HEA-HEO heterostructure. The dispersive X-ray spectroscopy (EDS) elemental mapping of the FeCoNiMnCr HEA-HEO/CNT sample shows a uniform distribution of Fe, Co, Ni, Mn, Cr, O, and C elements (Figure 2g; and Figure S8, Supporting Information). Furthermore, the Raman spectrum of the FeCoNiMnCr HEA-HEO/CNT sample shows two new peaks at ≈550–750 cm^{-1}, which are referred to M—O bonds (Figure S9, Supporting Information),[14] indicating a successful transition from HEA to HEA-HEO by the Cr-induced in situ construction strategy. The analyses of N_2 adsorption–desorption isotherms (Figure S10a, Supporting Information) and the pore size distribution curves (Figure S10b, Supporting Information) by the Brunauer, Emmett, and Teller (BET) and Barrett–Joyner–Halenda (BJH) method reveal that the FeCoNiMnCr HEA-HEO/CNT composite possesses a high BET surface area of 158.3112 $m^2\ g^{-1}$ and displays the coexistence of micropores and mesopores (Table S2, Supporting Information). The presence of abundant pores is expected to provide more catalytic active sites, facilitating charge and mass transport during electrocatalysis.

The X-ray photoelectron spectroscopy (XPS) analysis reveals the presence of Fe, Co, Ni, Mn, Cr, O, and C in the FeCoNiMnCr HEA-HEO/CNT catalyst, in good agreement with the EDS analysis (**Figure 3a**; and Table S3, Supporting Information).

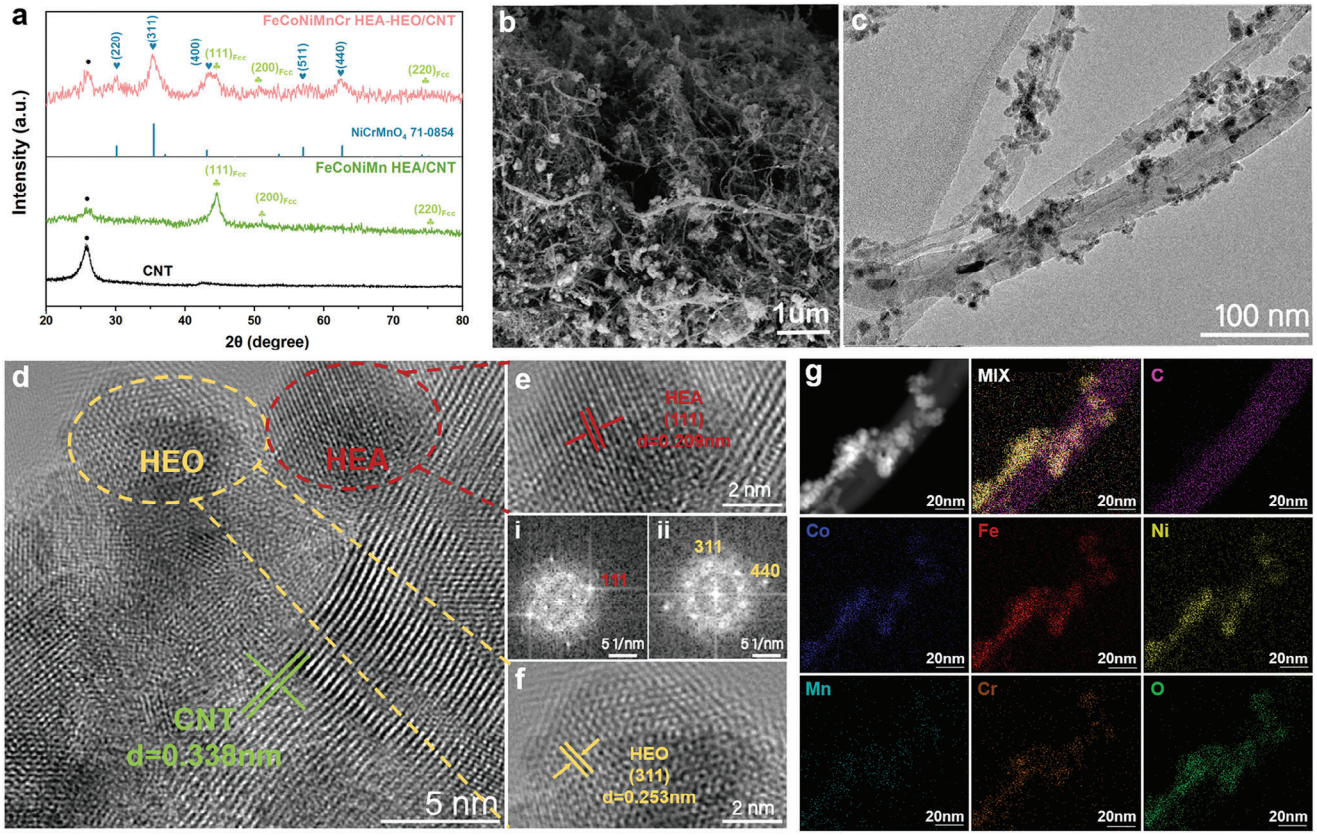

Figure 2. Synthesis and characterization of the FeCoNiMnCr HEA-HEO catalysts. a) XRD patterns of the FeCoNiMnCr HEA-HEO/CNT and FeCoNiMn HEA/CNT. b–d) SEM b), TEM c), and HRTEM d) images of the FeCoNiMnCr HEA-HEO/CNT. e,i) HRTEM image e) and the corresponding FFT schematic illustration (i) of the HEA (111) facet taken from the area marked in (d). f,ii) HRTEM image f) and the corresponding FFT schematic illustration (ii) revealing the presence of the HEO (311) facet taken from the area marked in (d). g) Elemental mapping of Fe, Co, Ni, Mn, Cr, C, and O in the FeCoNiMnCr HEA-HEO/CNT.

High-resolution C 1s XPS spectra further confirm the composition of CNT with distinct C═C/C—C species at 284.7 eV (Figure S11, Supporting Information).[16] The binding energies of Co $2p_{3/2}$ at 779.9 eV, Fe $2p_{3/2}$ at 710.3 eV, Ni $2p_{3/2}$ at 853.2 eV, and Mn $2p_{3/2}$ at 637.5 eV confirm the existence of metallic Co, Fe, Ni, and Mn in both the FeCoNiMn HEA/CNT and FeCoNiMnCr HEA-HEO/CNT catalysts (Figure 3b–e).[17] There emerge spin doublets at 576.53 eV (Cr^0 $2p_{3/2}$) and 577.75 eV (Cr^{3+} $2p_{3/2}$) in the Cr 2p spectrum of FeCoNiMnCr HEA-HEO/CNT, indicating the presence of metallic Cr and oxidative Cr^{3+} states in the FeCoNiMnCr HEA-HEO/CNT (Figure S12, Supporting Information). As shown in Figure 3f, it is obvious that the O 1s spectrum in FeCoNiMnCr HEA-HEO/CNT can be fitted to three peaks, which correspond to M—OOH (≈532.3 eV), M—OH (≈531 eV), and M—O (≈529.6 eV).[18] Unlike the FeCoNiMn HEA/CNT, there is an obvious lattice oxygen signal (M—O) in the FeCoNiMnCr HEA-HEO/CNT (Table S4, Supporting Information), further verifying the existence of the HEA-HEO heterostructure in the prepared FeCoNiMnCr HEA-HEO/CNT catalyst.

To gain insights into the chemical states of the FeCoNiMnCr HEA-HEO/CNT, we performed X-ray absorption fine structure (XAFS) analysis. From the X-ray absorption near edge structure (XANES), obvious metallic characteristics is observed in the HEA catalyst, while HEO catalyst exhibit more oxide features (Figure 3g). By comparing the absorption edge positions of the catalysts to the $Ni^{2+}(OH)_2$ and $LaNi^{3+}O_3$ references, we estimated mean valence state of HEA and HEO to be 0.8+ and 1.7+, respectively.[19] The Fourier transformed extended X-ray absorption fine structure (FT-EXAFS) was performed to extract the coordination structures of the catalysts. The coordination feature of HEA resembles that of Ni foil, showing an intense peak at ≈2.1 Å (phase uncorrected), which is assigned to the Ni—metal (Ni—M) coordination shell.[20] This is consistent with its low valence and confirms that most of Ni atoms in HEA are in metallic state. In comparison, there appears more Ni—O feature in HEO, verifying its heterostructure (Figure 3h). The quantitative structural fitting of HEO reveals the coordination number (CN) of Ni—O as 2.5 and Ni—M as 5.6 (Figures S14–S15 and Table S5, Supporting Information). The Ni—M in HEA shell has a larger coordination number of 7.7 as well as a small Ni—O coordination number of 1.0. The coordination number of Ni—M in the catalysts is remarkably smaller than that of Ni foil (CN = 12), which is ascribed to small particle size of the catalysts.[21] The wavelet transformations (Figure 3i) of HEA, HEO, and Ni foil show a strong feature centered at high R (Δk ≈4–10 $Å^{-1}$ and ΔR ≈1.7–2.5 Å) associated with the Ni—M shell. In $Ni(OH)_2$, the presence of a different feature at Δk ≈2–7 $Å^{-1}$ and ΔR ≈1.2–1.8 Å is attributed to Ni—O

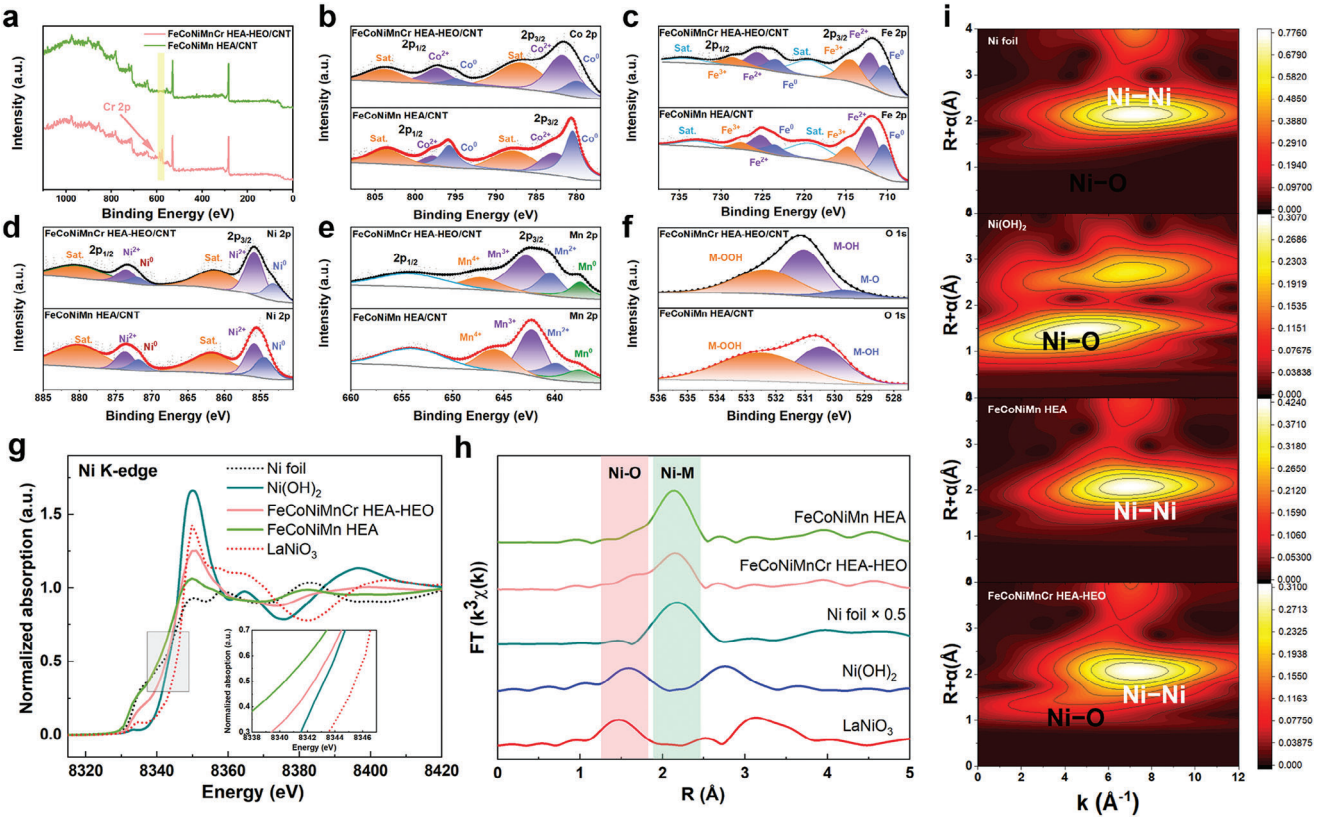

Figure 3. Chemical states analysis. a) XPS spectra of the FeCoNiMnCr HEA-HEO/CNT and FeCoNiMn HEA/CNT. b–f) High-resolution XPS spectra of Co 2p b), Fe 2p c), Ni 2p d), Mn 2p e), and O f) for the FeCoNiMnCr HEA-HEO/CNT and FeCoNiMn HEA/CNT. g) Ni K-edge XANES spectra. h) Ni K-edge EXAFS spectral of the FeCoNiMnCr HEA-HEO, FeCoNiMn HEA/CNT, and the references. i) The wavelet transform analysis of the FeCoNiMnCr HEA-HEO, FeCoNiMn HEA/CNT, NiO, and Ni-foil.

shell, which is also observed in HEO.[22] These results further confirm the coexistence of Ni—O and Ni—M shells in HEO.

2.2. Catalytic Activity of the FeCoNiMnCr HEA-HEO/CNT for OER

The electrocatalytic OER performances of the FeCoNiMnCr HEA-HEO/CNT and FeCoNiMn HEA/CNT catalysts together with those of the FeCoNiMnCr HEA/CNT, FeCoNiMnCr HEO/CNT, and commercial IrO_2 catalysts as a reference (Figures S16 and S17, Supporting Information) were investigated using a three-electrode system in O_2-saturated 1 M KOH solution at room temperature. As shown in the CV curve of the FeCoNiMnCr HEA-HEO/CNT (Figure S18, Supporting Information), there emerge redox peaks between 1.2 and 1.4 V, which are attributed to the redox of $Ni^{2+}(Fe^{2+})$, $Ni^{3+}(Fe^{3+})$, and $Ni^{4+}(Fe^{4+})$.[23] The FeCoNiMnCr HEA-HEO/CNT catalyst exhibits the lowest overpotential of 261 mV at a current density of 10 mA cm^{-2} (**Figure 4a**; and Figure S19, Supporting Information) and an ultralow overpotential of 320 mV at a high current density of 500 mA cm^{-2}, holding great potential for practical application. The Tafel slope of the FeCoNiMnCr HEA-HEO/CNT catalyst (42.2 mV dec^{-1}) is lower than that of FeCoNiMn HEA/CNT (51.76 mV dec^{-1}), FeCoNiMnCr HEA/CNT (52.33 mV dec^{-1}), and IrO_2 (107.27 mV dec^{-1}) (Figure 4b), implying a much faster OER kinetics on its surface. It is known that the electrochemical active surface area (ECSA) of an electrocatalyst is proportional to the electrochemical double-layer capacitance (C_{dl}), which can be evaluated by measuring scan-rate-dependent cyclic voltammetry (CV) in the non-Faraday region. As shown in Figure 4c; and Figure S20 (Supporting Information), the C_{dl} of the FeCoNiMnCr HEA-HEO/CNT catalyst is estimated to be 2.83 mF cm^{-2}, which approaches that of the FeCoNiMn HEA/CNT (7.21 mF cm^{-2}), FeCoNiMnCr HEA/CNT (1.00 mF cm^{-2}), and IrO_2 (6.04 mF cm^{-2}) catalysts. As shown in the ECSA normalized polarization curves (Figure S21, Supporting Information), the FeCoNiMnCr HEA-HEO/CNT catalyst exhibits the lowest overpotential at the kinetic current density of 1 mA $cm^{-2}{}_{ECSA}$. From Figure S22 (Supporting Information), the FeCoNiMnCr HEA-HEO/CNT catalyst displays the highest specific activity of 1.43 mA cm^{-2} at the overpotential of 300 mV in comparison to the synthesized FeCoNiMnCr HEA/CNT (1.05 mA cm^{-2}) and FeCoNiMn HEA/CNT (0.56 mA cm^{-2}) catalysts.

To further probe the electrode reaction kinetics during the catalytic OER process, we conducted the electrochemical impedance spectroscopy (EIS) measurement (Figure 4d). The Nyquist plots reveal that the FeCoNiMnCr HEA-HEO/CNT possesses the lowest charge transfer resistance (R_{ct}) of ≈1.81 Ω at the

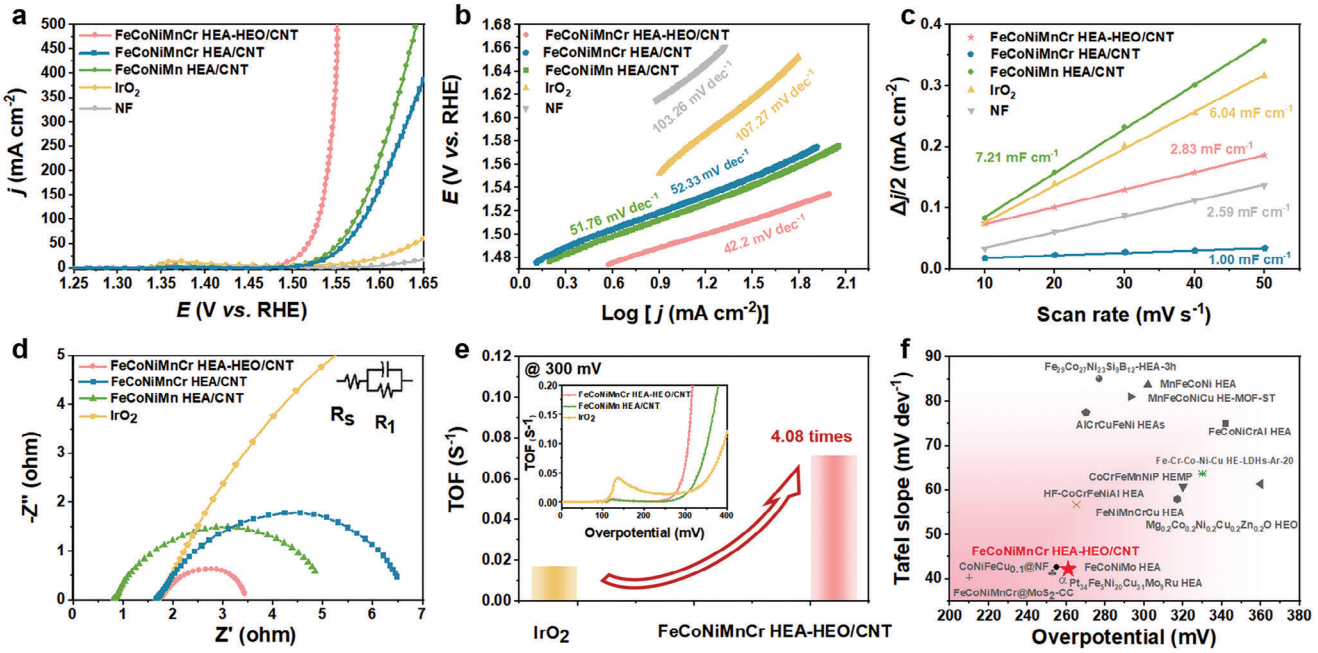

Figure 4. Electrocatalytic properties. a,b) IR-corrected polarization curves a) and Tafel plots b) of the FeCoNiMnCr HEA-HEO/CNT, FeCoNiMnCr HEA/CNT, FeCoNiMn HEA/CNT, and commercial IrO_2 catalysts measured in 1 M KOH solution at room temperature. c,d) Charging current density differences plotted against scan rate c) and Nyquist plots d) for the FeCoNiMnCr HEA-HEO/CNT, FeCoNiMnCr HEA/CNT, FeCoNiMn HEA/CNT, and commercial IrO_2 catalysts. e) Comparison of TOF for the FeCoNiMnCr HEA-HEO/CNT and the commercial IrO_2 catalysts at the overpotential of 300 mV. The inset shows the TOF plots of the FeCoNiMnCr HEA-HEO/CNT, FeCoNiMn HEA/CNT, and IrO_2 catalysts at different overpotentials. f) Comparison of overpotentials at 10 mA cm^{-2} and Tafel slopes for the FeCoNiMnCr HEA-HEO/CNT catalyst with the recently reported high-entropy OER electrocatalysts in 1 M KOH.

overpotential of 300 mV in 1 M KOH, much lower than the FeCoNiMn HEA/CNT (4.2 Ω), FeCoNiMnCr HEA/CNT (5.1 Ω), and IrO_2 (18.3 Ω), indicative of the highest electronic conductivity and the fastest charge transfer on its surface in the electrochemical OER process, which may be attributed to the increased exposed active sites formed on the HEA-HEO heterostructure and to the unusual electron configuration of Cr ion.[24] As shown in Figure 4e, the FeCoNiMnCr HEA-HEO/CNT catalyst displays an ultrahigh turnover frequency (TOF) of 0.0715 s^{-1} at the overpotential of 300 mV in an alkaline medium, which is 4.08 times higher than that of the commercial IrO_2 catalyst. Owing to the low overpotential and small Tafel slope, the OER activity of FeCoNiMnCr HEA-HEO/CNT also surpasses many of the recently reported high-entropy electrocatalysts under the same conditions (Figure 4f; and Table S6, Supporting Information).[8,25] The OER electrocatalytic performance of the FeCoNiMnCr HEA-HEO/CNT catalyst in neutral medium (1 M PBS electrolyte) differs from that in alkaline medium (Figure S23, Supporting Information). To probe the comprehensive water decomposition efficiency of the FeCoNiMnCr HEA-HeO/CNT catalyst, we conducted analysis of the water electrolysis performance of the specimen, as sketched in Figure S24 (Supporting Information). Gas output was obtained using the drainage method at a current density of 100 mA cm^{-2} (Figure S25, Supporting Information). The yield of O_2 and the volume ratio of H_2 and O_2 (H_2:O_2 = 2:1) approach closely their theoretical values (Figure S26, Supporting Information), indicating an almost 100% Faradaic efficiency (FE) of the catalyst.

2.3. Catalytic Stability of the FeCoNiMnCr HEA-HEO/CNT for OER

For an electrocatalyst to be used in practical scenario, it is essential for it to maintain good durability over long-term use, especially when operating at high current densities. To further investigate stability of the FeCoNiMnCr HEA-HEO/CNT, we performed chronopotentiometry tests. From **Figure 5a**, one can see that the potential at the current density of 100 mA cm^{-2} for 100 h undergoes no change, indicating good long-term stability of the FeCoNiMnCr HEA-HEO/CNT catalyst toward OER. Surprisingly, the electrocatalytic activity of FeCoNiMnCr HEA-HEO/CNT is even enhanced after 100 h at 100 mA cm^{-2}. The overpotential is reduced to 247 mV at the current density of 10 mA cm^{-2}, which is 14 mV lower than that of its initial value (Figure 5b). The enhancement of OER electrocatalytic performance for the FeCoNiMnCr HEA-HEO/CNT catalyst after stability test may be ascribed to the slightly increased ECSA of the posttest catalyst (Figure S27, Supporting Information). Further XRD analysis reveals no obvious change in crystalline structure for the FeCoNiMnCr HEA-HEO/CNT catalyst after stability test for 100 h at 100 mA cm^{-2} (Figure 5c). Moreover, morphology of the catalyst after the stability test is essentially identical to that before test (Figure S28, Supporting Information). From the HRTEM images in Figure 5e–g, one can note that the (111) plane of HEA and the (311) plane of HEO experience insignificant lattice expansion, indicating that the HEA-HEO heterostructure in the FeCoNiMnCr HEA-HEO/CNT catalyst is well preserved after long-term

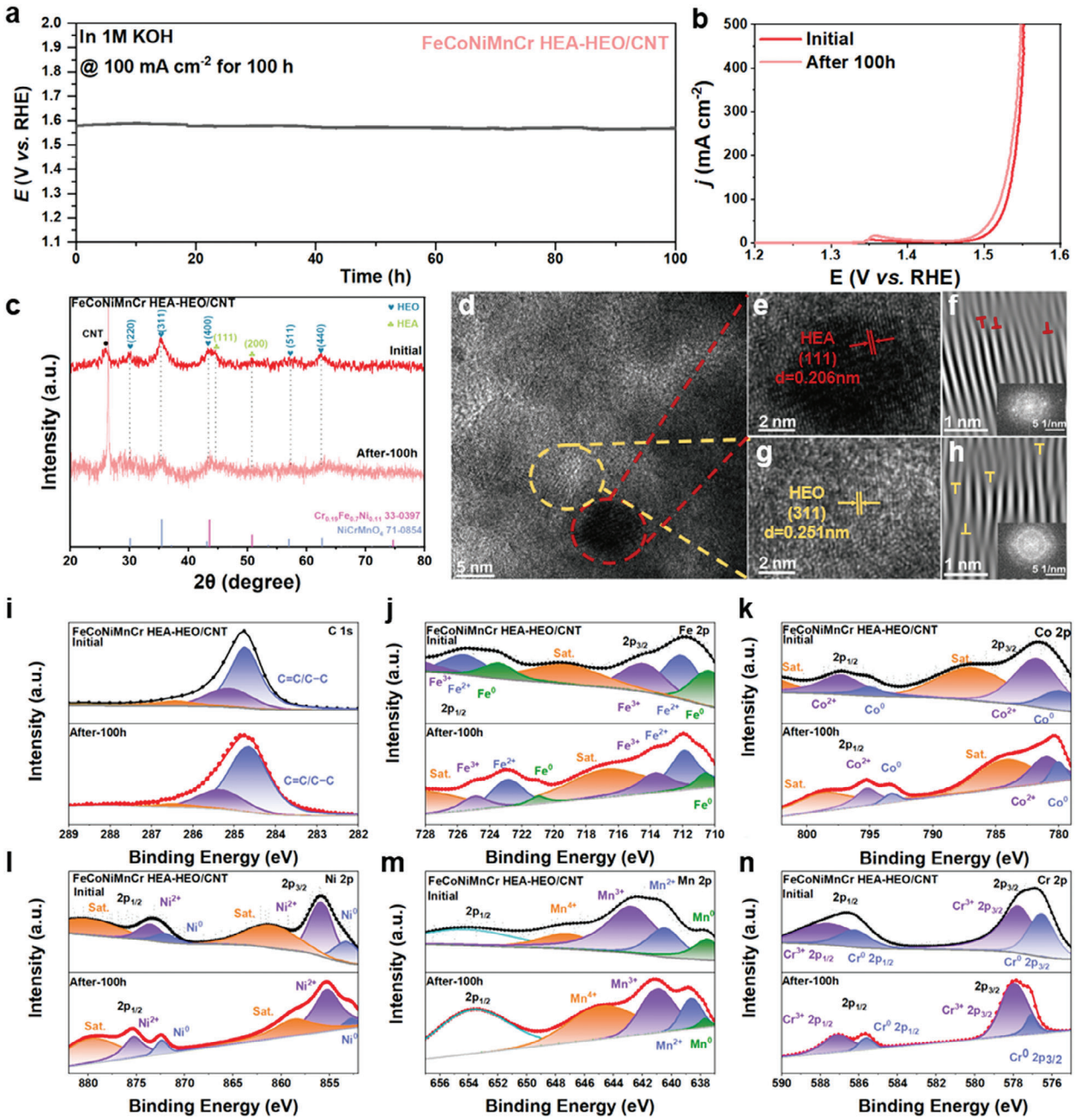

Figure 5. Electrocatalytic OER stability and structural characterization of the FeCoNiMnCr HEA-HEO/CNT catalyst in 1 M KOH at 100 mA cm^{-2} for 100 h. a) Catalytic stability measured by chronopotentiometry in 1 M KOH at room temperature. b) Polarization curves before and after the stability test. c,d) XRD pattern c) and HRTEM image d) of the FeCoNiMnCr HEA-HEO/CNT after stability test for 100 h at 100 mA cm^{-2}. e,f) HRTEM image e) and atomic lattice image f) of the selected areas marked by a red circle in (d). The inset in (f) shows the corresponding FFT. g,h) HRTEM image g) and atomic lattice image h) of the selected areas marked by a yellow circle in (d). The inset in (h) shows the corresponding FFT. i–n) High-resolution XPS spectra of C 2p i), Fe 2p j), Co 2p k), Ni 2p l), Mn 2p m), and Cr 2p n) of the FeCoNiMnCr HEA-HEO/CNT catalyst before and after stability test for 100 h at the current density of 100 mA cm^{-2} in 1 M KOH.

stability test. In addition, there also appear dislocations in the catalyst (Figure 5f,h), and the Fe, Co, Ni, Mn, Cr, C, and O elements remain evenly distributed throughout the whole region of the FeCoNiMnCr HEA-HEO/CNT catalyst after stability test (Figure S29, Supporting Information). To further probe structure of the catalyst after stability test, the high-resolution XPS spectra are obtained, which show the similar deconvoluted peaks with the spectra before test (Figure 5i–n; and Figure S30, Supporting Information), confirming no obvious structural change for the FeCoNiMnCr HEA-HEO/CNT during the OER electrocatalysis. Compared to the FeCoNiMnCr HEA-HEO/CNT before stability test (9.7 at%), the proportion of M–O (lattice oxygen) for

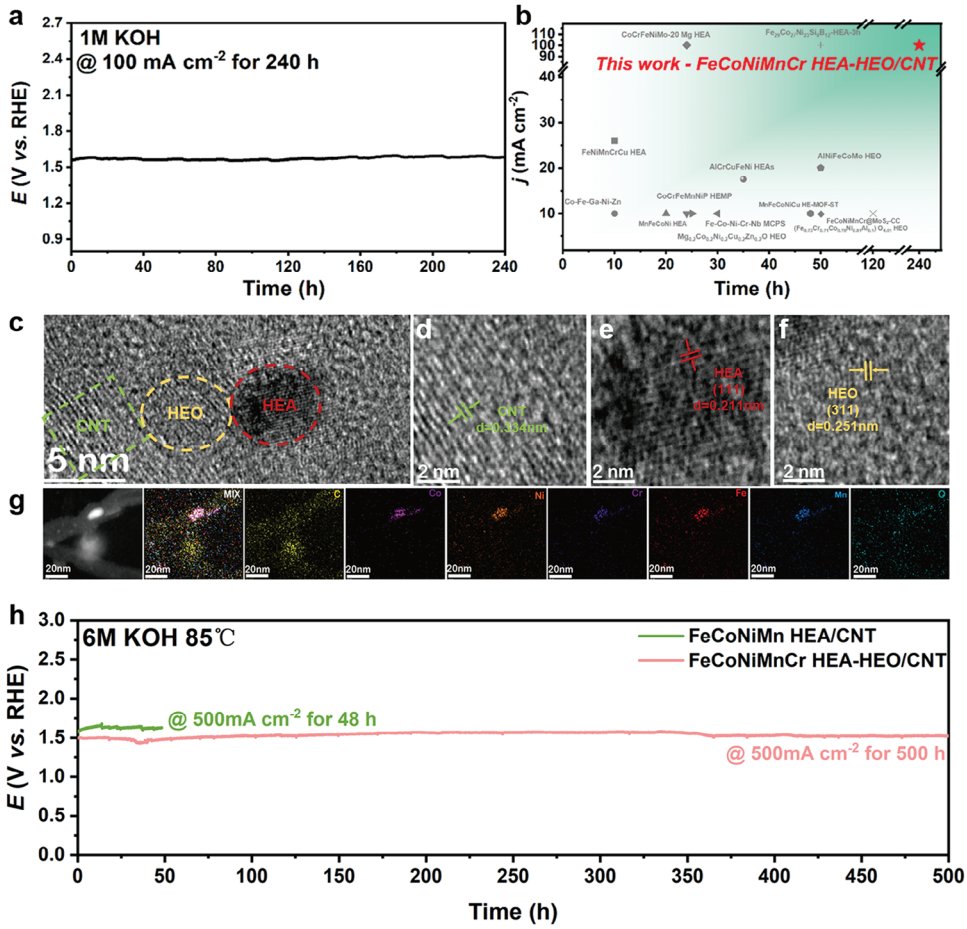

Figure 6. Structure and catalytic long-term stability of the FeCoNiMnCr HEA-HEO/CNT catalyst. a) Catalytic stability test by chronopotentiometry measurement in 1 M KOH at room temperature. b) Comparison of stability for the FeCoNiMnCr HEA-HEO/CNT catalyst with the recently reported high-entropy OER electrocatalysts in 1 M KOH. c) HRTEM image of the FeCoNiMnCr HEA-HEO/CNT after stability test for 240 h at 100 mA cm^{-2}. d–f) Enlarged HRTEM image of the CNT, HEA, and HEO taken from the area marked in (c). g) Elemental mapping of the FeCoNiMnCr HEA-HEO/CNT catalyst after stability test for 240 h at 100 mA cm^{-2}. h) Catalytic stability test of the FeCoNiMnCr HEA-HEO/CNT and FeCoNiMn HEA/CNT at 500 mA cm^{-2} under industrial conditions of 6 M KOH and 85 °C.

FeCoNiMnCr HEA-HEO/CNT after stability test at 100 mA cm^{-2} for 100 h (16.02 at%) increases, indicating the generation of newly formed oxides in the FeCoNiMnCr HEA-HEO/CNT surface during the OER process (Table S4, Supporting Information). These indicate that the metallic and oxidation states of the FeCoNiMnCr HEA-HEO/CNT catalyst are well preserved during the OER process.

The OER stability test is further carried out at 100 mA cm^{-2} for 240 h, which shows no degradation during the OER process even after 10 days, indicating a long-term stability of the FeCoNiMnCr HEA-HEO/CNT catalyst (**Figure 6**a,b; and Table S6, Supporting Information). The FeCoNiMnCr HEA-HEO/CNT catalyst maintains the nanoparticle morphology after the stability test (Figure 6c; and Figure S31, Supporting Information). The HRTEM images in Figure 6d–f further clearly show the (002) plane of the CNT, (111) plane of HEA, and (311) plane of HEO, indicating that microstructure of the catalyst is stable even after the long-term stability test for 240 h. Moreover, the TEM mapping also shows the similar distribution of the Fe, Co, Ni, Mn, Cr, C, and O elements before and after stability test, verifying that the HEA-HEO heterostructure in the catalyst is well preserved during the long-term OER process (Figure 6g).

To test practical application of the catalyst, we further conducted stability test under harsh industrial conditions (6 M KOH and 85 °C). As shown in Figures S32–S35 (Supporting Information), the FeCoNiMnCr HEA-HEO/CNT catalyst shows no decay in both the OER performance and ECSA of after maintaining at 100 mA cm^{-2} for 24 h in 6 M KOH at 85 °C. Furthermore, the chronopotentiometric curve of the catalyst exhibits no obvious potential increase even after stability test for 500 h at 500 mA cm^{-2} (Figure 6h). The polarization curves before and after 500 h stability test exhibit only 12 mV increase in the overpotential at 500 mA cm^{-2}, which is much better than that of the FeCoNiMn HEA/CNT catalyst showing an overpotential increase of 23 mV after 48 h stability test at 500 mA cm^{-2} (Figures S36–S39, Supporting Information). The stability of the FeCoNiMnCr HEA-HEO/CNT catalyst outperforms most of the current noble-metal-free OER catalysts (Table S7, Supporting Information).

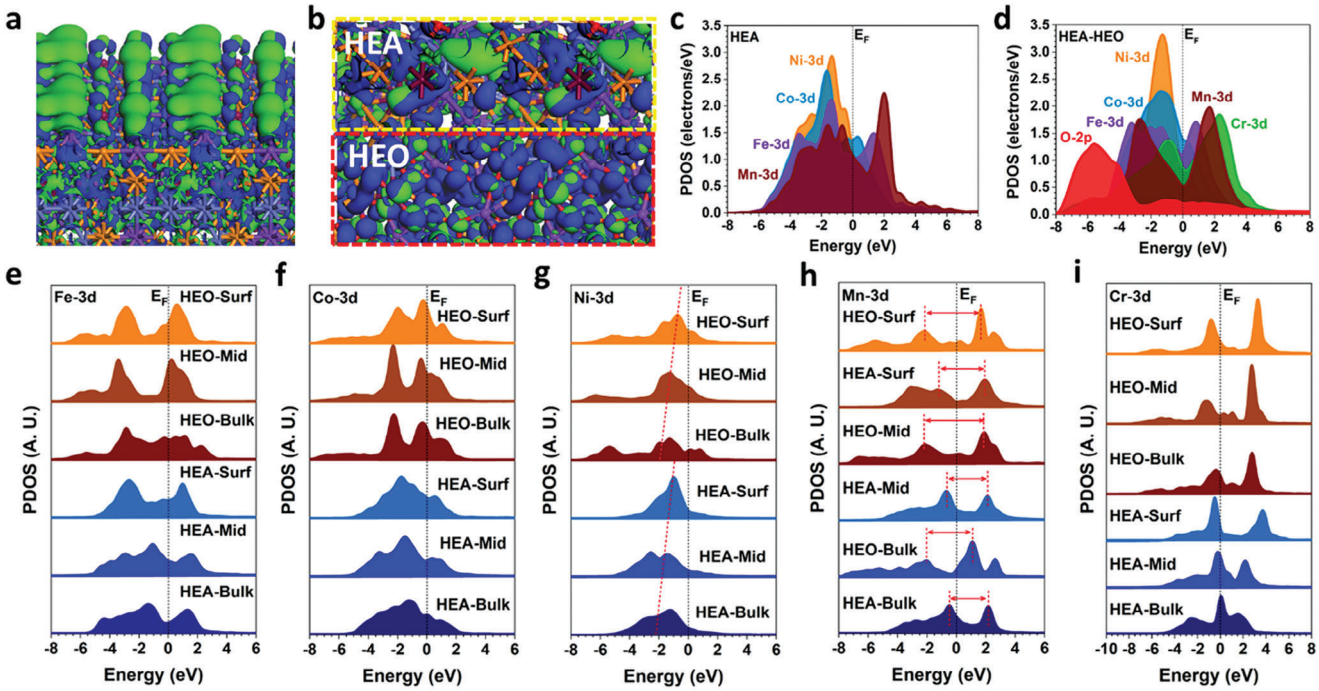

Figure 7. Electronic structure. a,b) 3D contour plot of electronic distribution near the Fermi level for the HEA a) and HEA-HEO b). In (b), the upper yellow rectangle denotes HEA and the bottom red one denotes HEO. The purple, blue, orange, brown, and gray balls represent Fe, Co, Ni, Mn, and Cr atoms, respectively. The blue isosurface represents bonding orbitals, and the green one antibonding orbitals. c,d) The projected density of states (PDOS) of HEA c) and HEA-HEO d). e–i) Site-dependent PDOS of of Fe-3d e), Co-3d f), Ni-3d g), Mn-3d h), and Cr-3d i).

3. Discussion

We further performed DFT calculations to investigate the electronic states of the FeCoNiMnCr HEA-HEO structure during the OER process. Based on the interface orientations observed from the HRTEM image, we constructed atomic models of the HEA/HEO interface by taking the (111) and (311) surfaces for HEA and HEO, respectively. To construct interfaces, strain is inevitably induced between the HEO and HEA due to their lattice mismatch. To shed light on the impact of strain, we compared bond length distribution in HEA, HEO, and HEA-HEO (Figure S31a, Supporting Information). For the pristine HEA, we note that the bond lengths are mostly in the range of ≈2.4–2.5 Å. The lattice distortion in the HEA results in the extension of bond lengths to even 3.2 Å. After the formation of the HEA-HEO, the bond length distribution turns smaller, where most of bond lengths are in the range of ≈2.4–2.8 Å indicating the presence of compressive strain in the HEA due to the formation of HEO. On the other hand, the bond lengths in the pristine HEO are limited to a smaller range of ≈1.8–2.1 Å. However, with the formation of the HEA-HEO interface, the strain effect triggers prolonged bonding in HEO, indicating that tensile strain is induced in the HEO component. The surface of the FeCoNiMnCr HEA structure is largely dominated by the antibonding orbitals (**Figure** 7a). In comparison, the formation of HEO induces increased electron-rich surface, which guarantees efficient electron transfer (Figure 7b). Moreover, the distortion of the HEA-HEO becomes slightly stronger due to the formation of HEO, consistent with the expanded peaks in the XRD results. These also indicate the existence of strain effect at interface, which could also potentially modify electronic structures of the HEA-HEO. For the HEA, all the 3*d* orbitals of different metals show a strong overlap, suggesting a strong *d*–*d* coupling within the lattice (Figure 7c). However, such an electronic structure potentially leads to a trade-off between the stable valence states of the key active sites and the stability. In contrast, the HEA-HEO displays a less overlap effect on the 3*d* orbitals due to the formation of HEO (Figure 7d). Both Ni 3*d* and Co 3*d* orbitals upshift slightly compared to those in HEA, indicating higher electroactivity. Meanwhile, the Fe 3*d* and Mn 3*d* are modulated, while the introduced Cr 3*d* orbitals shift in position from Mn-3d orbitals. Such orbital shift not only guarantees high electron density near the Fermi level (E_F), but also fully covers the highly electroactive 3*d* orbitals of Ni and Co to achieve robust valence states during the long-term OER. The O 2*p* orbitals locate at the lowest level as the electron reservoir center. For the HEA-HEO interface, the electron density increases in HEO yet decreases in HEA, which supports the experimental results (Figure S31b, Supporting Information).

The site-dependent projected density of states (PDOS) is further investigated by analyzing different elements in HEA-HEO. For the Fe 3*d* orbitals, the formation of HEO induces the broadening of Fe 3*d* orbitals with increased e_g-t_{2g} splitting (Figure 6e). The broadened Fe 3*d* orbitals enable the pinning of Ni sites to maintain robust valence states during OER. The Co 3*d* orbitals are evidently modulated after the formation of HEO, where the 3*d* orbitals turn shaper with increased electron density near the Fermi level, supporting the improved electroactivity in HEA-HEO (Figure 7f).

Within the HEA-HEO, we notice that the Ni-3*d* orbitals exhibit much broader 3*d* orbitals in the HEA than in the HEO

(Figure 7g). From the bulk to surface, the 3*d* orbitals gradually upshifts to boost the electroactivity on the surface Ni sites for the OER. For the Mn-3*d* orbitals, the e_g-t_{2g} splitting is evidently enlarged in the HEO, and the expanded Mn-3d orbitals are able to pin the active 3*d* orbitals to reach stable electroactivity (Figure 7h). Similarly, it is noted that the Cr-3*d* orbitals are obviously broadened in the HEO, which facilitates the site-to-site electron transfer within the HEA-HEO. The pinning of Ni and Co sites enables long-term electroactivity (Figure 7i). Due to the synergistic effect of different transition metals, the pinning of Ni and Co sites can be fulfilled by optimizing electronic structures, enabling long-term electroactivity for OER. The evident electronic modulation induced by the formation of HEO is able to improve the electroactivity and electron transfer efficiency of the bulk to accelerate OER process. The formation of HEO thus modifies remarkably electronic structures through the dislocation effect on the 3*d* orbitals, leading to improved and more robust electroactivity to guarantee a long-term efficient OER process.

To shed light on origin of the enhanced OER performance for the FeCoNiMnCr HEA-HEO/CNT and the effect of electron transfer on binding strength of reactants and intermediates during OER, we adopted methanol as a probe to detect adsorption ability of the OER intermediates, e.g., OH^* which is an electrophilic reagent and can be easily captured by the nucleophilic methanol. Therefore, the increase in current density between the methanol oxidation reaction (MOR) and OER polarization curves reflects the coverage of OH* on the catalyst surface.[26] As shown in **Figure 8a**; and Figure S41 (Supporting Information), the current difference caused by the MOR can reflect the extent of surface coverage of OH* to further embody the OH^* adsorption ability. The filled areas between the LSV curves with and without methanol for the FeCoNiMnCr HEA/CNT (S_1), FeCoNiMnCr HEA-HEO/CNT (S_2), FeCoNiMn HEA/CNT (S_3), and FeCoNiMnCr HEO/CNT (S_{HEO}), are calculated to be $S_1 = 3.02$, $S_2 = 2.74$, $S_3 = 5.71$, and $S_{HEO} = 0.638$, indicating that the FeCoNiMn HEA/CNT has the highest absorption strength toward OH^*, followed by the FeCoNiMnCr HEA/CNT, FeCoNiMnCr HEA-HEO/CNT, and FeCoNiMnCr HEO/CNT.

The CV curves for the FeCoNiMn HEA/CNT, FeCoNiMnCr HEA/CNT, FeCoNiMnCr HEA-HEO/CNT, and FeCoNiMnCr HEO/CNT catalysts show little difference between the electrolytes with and without methanol in various scan rates, indicating that the increase of the MOR current is not related to the ECSA (Figure S42, Supporting Information). From the energetic perspective, we also compared the adsorption energies of OH^* on the FeCoNiMn HEA/CNT FeCoNiMnCr HEA-HEO/CNT surface and FeCoNiMnCr HEO/CNT (Figure 8b). Notably, the HEA shows the strongest binding strength of OH*, while the HEO the weakest binding strength, which supports the experimental characterizations. The relatively stronger adsorption of OH* in the HEA than the pristine HEO are beneficial to further conversion of key intermediates, indicating its much higher OER performance than that of HEO. For the pristine HEO interface, the adsorption of the OH* still shows strong electron accumulation, which indicates a weak electron transfer with the catalysts, resulting in the weak adsorption with limited electroactivity for the pristine HEO (Figure S40c, Supporting Information). In comparison, the electron density of OH* shows a decreasing trend toward the surface Ni sites on the HEA, which demonstrates stronger electron transfer from OH* to the HEA surface with the improved oxidation trend for the OER process (Figure S40d, Supporting Information). For the adsorption of OH* on the Ni sites at the HEA-HEO interface, the electron transfer is evident from OH* to catalyst surface, meaning an efficient oxidation process to accelerate the conversion from OH* to O* (Figure S40e, Supporting Information). The MOR analysis and DFT calculations reveal a moderate adsorption of the OER intermediates on the designed FeCoNiMnCr HEA-HEO/CNT catalyst surface, indicating an optimized OER electrocatalytic activity and stability for this catalyst. In addition, we have also compared the work functions of three different systems as well as the HEA and HEA-HEO (Figure 8c). It is noted that the HEA-HEO shows a middle work function between the pristine HEA surface and the pristine HEO surface, suggesting the formation of built-in electric field (BEF) in the HEA-HEO. The formed BEF with different work function would drive electron flow from HEA to the HEO, benefiting the electroactivity toward the OER.

To further probe the active sites of HEA-HEO, we calculated the free energy of the HEA-HEO, HEA, and HEO, where the reaction energies are calculated without applied potential (U = 0 V) (Figure 8d–f). On the HEA surface, a lower energy is required for the initial conversion from OH^- to OH^*, consistent with the experimental results on the methanol probe. Meanwhile, we notice that the rate-determining step (RDS) is the conversion from O* to OOH* for all the metal sites on different surfaces. For the HEA surface, all the reaction steps have delivered relatively high energy barriers except for the final step (Figure 8d). Among the different metal sites, Ni sites show the smallest energy barrier for RDS, serving as the most promising active sites for OER. For the interface of FeCoNiMnCr HEA-HEO, the energy cost for the OH* formation is slightly increased, while the conversion to O* and OOH* is significantly alleviated, supporting the adsorption energy results (Figure 8e). In particular, the Ni sites display the highest electroactivity with the smallest overpotential, in line with the PDOS results. As a comparison, we also evaluated the OER trends on the pristine HEO surfaces, where the overpotential for OER is evidently increased, indicating that the improved OER performance is also attributed to the formation of highly electroactive HEA-HEO interface after introducing Cr (Figure 8f). Based on the analysis of reaction energy, the Ni is the most electroactive site to promote OER, where the HEA-HEO shows the lowest RDS barrier of 1.52 eV.

Furthermore, due to the dependency between free energy of the reaction intermediates and the OER activity, the change of Gibbs free energy in each elementary step was calculated to explore the improvement of OER performance by applying the equilibrium potential of 1.23 V for Ni sites of HEA and HEA-HEO interface (Figure 8g). The optimized adsorption structures of the reaction intermediates (OH*, O*, OOH*) on the catalyst surface are also supplied. Notably, for HER-Ni, the electrocatalyst experiences a gradual uphill trend for OER, where the barrier of RDS requires an overpotential of 0.48 V. With the formation of the HEO, although the initial formation of OH* can satisfy the barrier, the RDS barrier reduces with significantly lowered overpotential of 0.29 V. Such reaction energy results therefore verify the remarkable OER performance of HEA-HEO. Compared with individual HEA and HEO surfaces, the interactions between

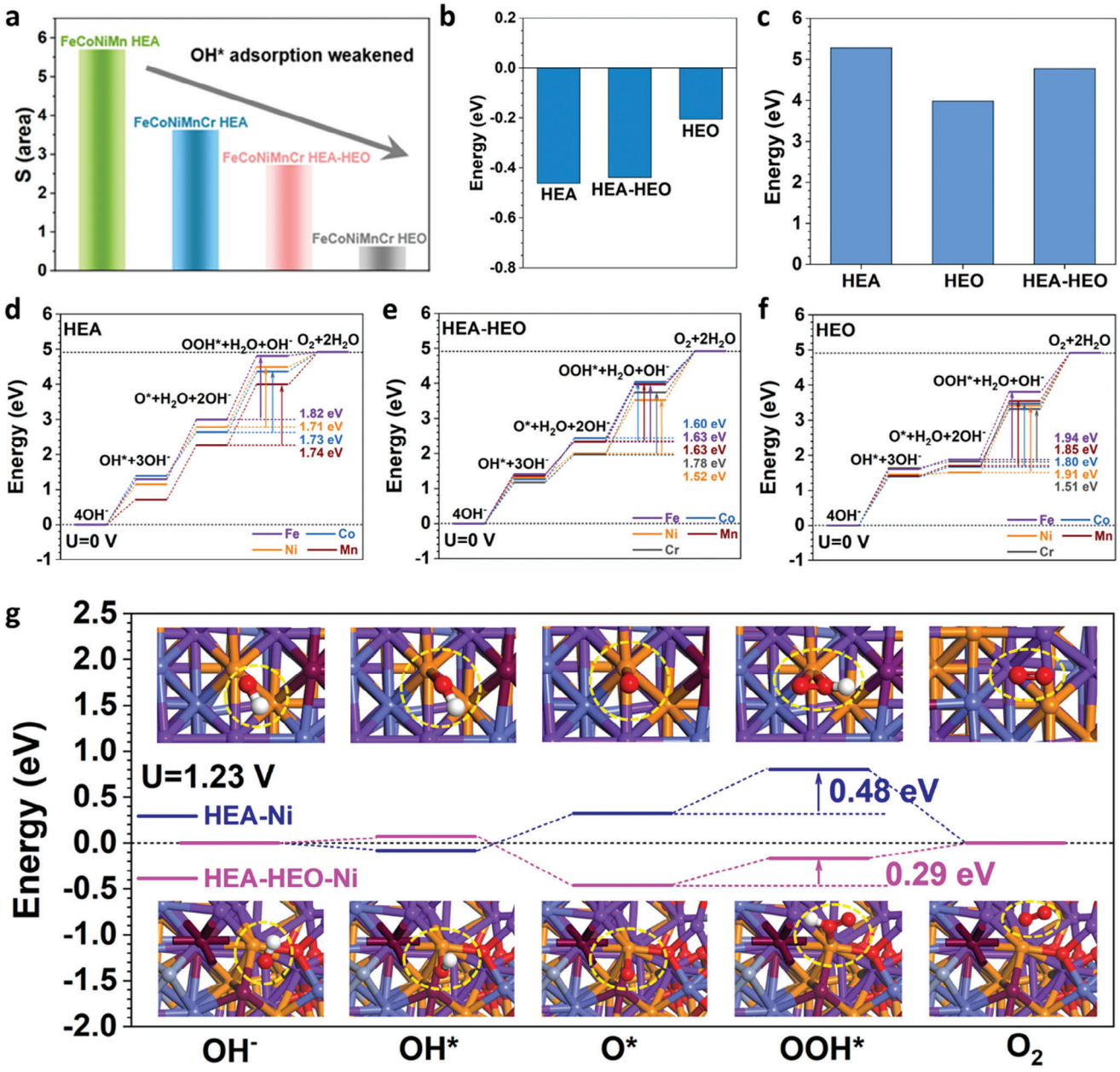

Figure 8. OER Mechanism. a) Comparison of the filled area caused by MOR for the FeCoNiMn HEA/CNT, FeCoNiMnCr HEA/CNT, FeCoNiMnCr HEA-HEO/CNT, and FeCoNiMnCr HEO/CNT catalysts. b) The binding energies of OH* on the FeCoNiMn HEA, FeCoNiMnCr HEO, and FeCoNiMnCr HEA-HEO. c) Comparison of work function for the FeCoNiMn HEA, FeCoNiMnCr HEO, and FeCoNiMnCr HEA-HEO. Reaction energies of OER on FeCoNiMn HEA d), FeCoNiMnCr HEO e), and FeCoNiMnCr HEA-HEO f) under U = 0 V. g) Reaction energy of OER on Ni site of the FeCoNiMn HEA and FeCoNiMnCr HEA-HEO under an equilibrium potential of U = 1.23 V. The purple, blue, orange, brown, and gray balls represent Fe, Co, Ni, Mn, and Cr atoms, respectively.

HEO and HEA result in optimization of electronic structures, which can further benefit the OER processes with reduced energy barriers and overpotentials.

We conducted in situ Ni K-edge XAFS studies to track the active structures of the catalysts under the applied potentials (**Figure** 9a–c). The energy position of the absorption edge of HEO catalyst is shifted to higher energy at applied potentials, i.e., the spectra show a distinct edge shift of ≈1.1 eV under catalytic potential of 1.50 V, giving a mean valence state of ≈2.2+ (Figures S43 and S44, Supporting Information). This indicates that a large proportion of Ni ions are oxidized into high valence states during the OER process. To verify this result, the FT-EXAFS analysis was performed. As expected, the Ni−M coordination number clearly decreases from 5.6 to 3.1 at an applied potential of 1.50 V, which is accompanied with the increase of Ni−O coordination, indicating that a substantial proportion of Ni atoms are transformed from the HEA phase to their oxidized states. A similar behavior is observed in HEA catalyst, in which the absorption edge shows a

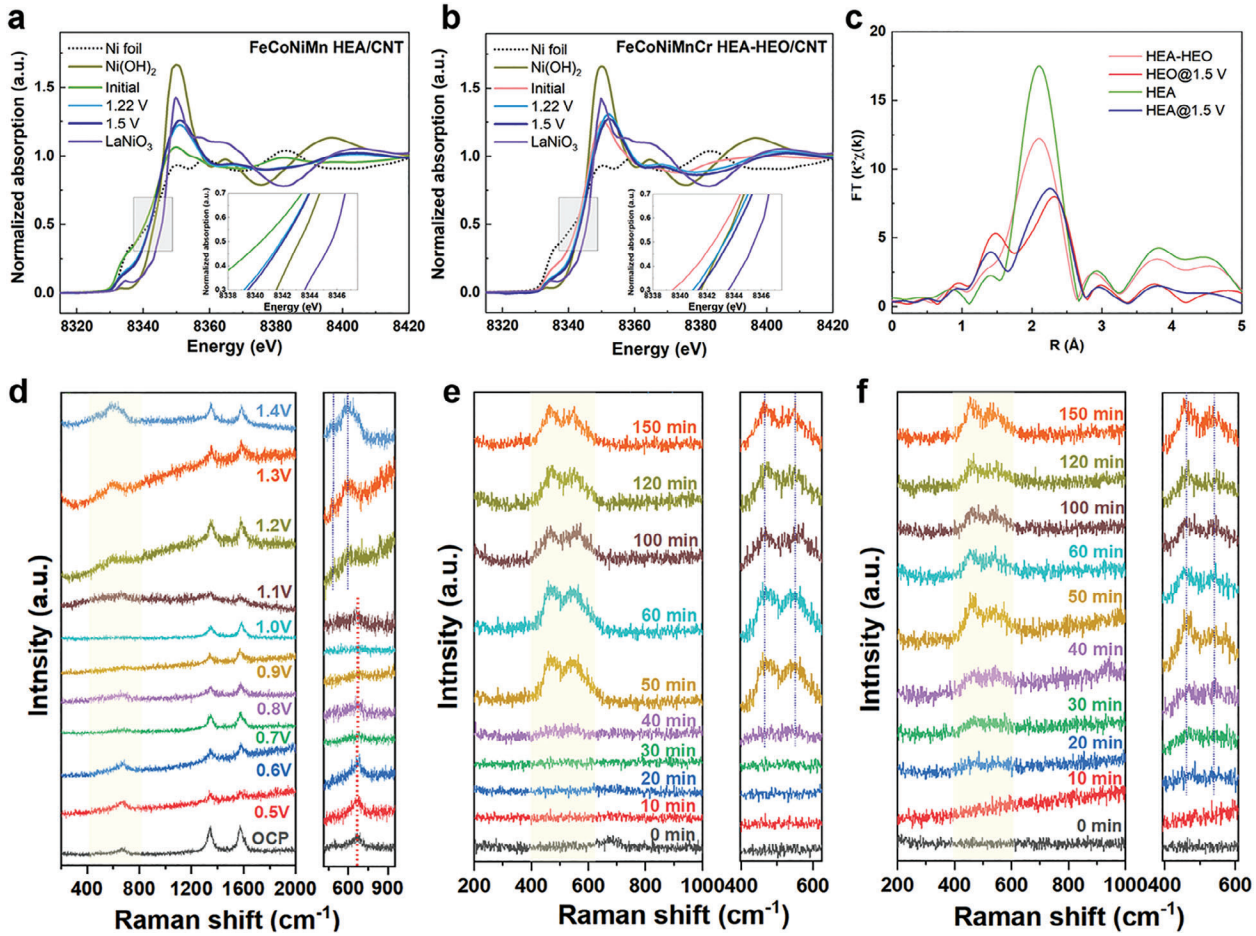

Figure 9. Operando analyses. In situ Ni K-edge XANES spectra of a) FeCoNiMn HEA/CNT and b) FeCoNiMnCr HEA-HEO/CNT catalysts at 1.22 and 1.5 V versus RHE. c) In situ Ni K-edge EXAFS spectra of FeCoNiMn HEA/CNT and FeCoNiMnCr HEA-HEO/CNT catalysts. In situ Raman spectra of FeCoNiMnCr HEA-HEO/CNT catalyst d) at different potentials (Versus Hg/HgO) catalysts and e) maintaining at 1.4 V versus Hg/HgO for different time. f) In situ Raman spectra of FeCoNiMn HEA/CNT catalyst maintaining at 1.4 V versus Hg/HgO for different time.

positive shift. The average valence state of Ni ions in HEA at 1.50 V versus RHE is estimated to be ≈1.5+.

We also performed in situ electrochemical Raman spectroscopy to investigate structural changes of FeCoNiMnCr HEA-HEO/CNT during the OER process. As shown in Figure 9d, there is no change in Raman response at voltage below 1.1 V versus Hg/HgO in 1 M KOH, indicating the preservation of original structure for FeCoNiMnCr HEA-HEO/CNT catalyst at low voltages. When the applied voltage is below to 1.1 V versus Hg/HgO, the FeCoNiMnCr HEA-HEO/CNT shows one well-defined peak at 671 cm^{-1}, which is attributed to the M–O (M=Fe, Co, Ni, Mn, Cr) vibrational mode. As shown in Figure S45 (Supporting Information), there is no detectable Raman response of FeCoNiMn HEA/CNT at 671 cm^{-1}, indicating its metallic nature. When the voltage is increased from 1.2 to 1.4 V versus Hg/HgO, the initial Raman peak at 671 cm^{-1} for FeCoNiMnCr HEA-HEO/CNT disappears, followed by the growth of a pair of new peaks at 475 cm^{-1} (δ (Ni^{III}–O) and 552 cm^{-1} (ν (Ni^{III}–O)), which are ascribed to the e_g bonding vibration and the A_{1g} stretching vibration bonds of Ni(FeCo)OOH, respectively, indicating the structural reconstruction of catalyst during the OER process. As shown in Figure S45 (Supporting Information), the Raman peaks at 475 and 552 cm^{-1} are formed at 0.9 V versus Hg/HgO for FeCoNiMn HEA/CNT catalyst, which is 0.3 V lower than that of FeCoNiMnCr HEA-HEO/CNT. In situ Raman characterization was further conducted to probe structural reconstruction of these two catalysts at a constant voltage of 1.4 V versus Hg/HgO under different time (Figure 9e,f). It is worthy of noting that the peaks of δ (Ni^{III}–O) at 475 cm^{-1} and ν (Ni^{III}–O) at 552 cm^{-1} for FeCoNiMnCr HEA-HEO/CNT appear after OER test for 40 min, which is 20 min later than that of the FeCoNiMn HEA/CNT catalyst. This agrees with the potential-dependent in situ Raman analysis, suggesting superior durability of the FeCoNiMnCr HEA-HEO/CNT catalyst.

4. Conclusions

We proposed an in situ reconstruction strategy to synthesize ultrastable HEA-HEO heterostructural OER catalysts, and demonstrated that the high-entropy composition can be adjusted between their metallic and oxide states by the Cr-induced spontaneous reconstruction. We show that the FeCoNiMnCr HEA-

HEO heterocatalyst is stable for over 500 h at 500 mA cm^{-2} under harsh industrial conditions of 6 M KOH and 85 °C. DFT calculations unravel that the formation of HEO induces an orbital dislocation effect to loosen to the 3d orbital pinning, which not only offers highly electroactive active sites but also promotes the site-to-site electron transfer, leading to the suitable intermediate binding strength for the OER process. Such an in situ reconstruction strategy from HEA to HEA-HEO heterostructure for building highly stable OER electrocatalysts represents an advancement toward further development of practical industrial water splitting.

5. Experimental Section

Sample Preparation: The FeCoNiMnCr MOFs/CNT was synthesized by dissolving 0.25 mmol ($Fe(CO_2CH_3)_2{\cdot}4H_2O$), 0.25 mmol $Co(NO_3)_2{\cdot}6H_2O$, 0.25 mmol $Ni(NO_3)_2{\cdot}6H_2O$, 0.25 mmol $Mn(NO_3)_2{\cdot}4H_2O$, 0.25 mmol $Cr(NO_3)_3{\cdot}9H_2O$, and 0.34 mmol 2,5-dihydroxyterephthalic acid into a mixture of 22.5 mL DMF, 1.35 mL anhydrous ethanol, and 1.35 mL deionized water. 25 mg carbon nanotubes were added into the mixture and sonicated for at least 60 min. Subsequently, the mixture was immediately transferred into a 50 mL autoclave, and heated to 120 °C and maintained for 30 h. The synthesized FeCoNiMnCr MOFs/CNT precursor was washed with ultrapure DI water, DMF, and EtOH in sequence several times, and dried at 70 °C for 12 h. Similarly, the FeCoNiMn MOFs/CNT precursor was synthesized using the same procedure except that the $Cr(NO_3)_3{\cdot}9H_2O$ was not added.

The FeCoNiMn HEA/CNT and FeCoNiMnCr HEA-HEO/CNT samples were obtained by pyrolysis of MOFs/CNT precursors in a tube furnace pretreated at 350 °C for 1 h. The sample was then heated to 450 °C at a ramp rate of 5 °C min^{-1} and maintained at this temperature for 2 h under mixed gas H_2/Ar (5% H_2). The FeCoNiMnCr HEA/CNT sample was obtained by pyrolysis of the FeCoNiMnCr MOFs/CNT precursors in a tube furnace at 350 °C for 1 h. The sample was then heated to 500 °C at a ramp rate of 5 °C min^{-1} and finally maintained at this temperature for 7 h under mixed gas H_2/Ar (5% H_2). Similarly, the FeCoNiMnCr HEO/CNT sample was obtained by pyrolysis of the FeCoNiMnCr MOFs/CNT precursors in air at 600 °C for 3 h.

Structural Characterization: The XAFS spectra at the Ni K-edge were recorded at the BL11B beamline of Shanghai Synchrotron Radiation Facility (SSRF). Powder X-ray diffraction (XRD) patterns were recorded using a Rigaku D/Max-2200 PC diffractometer in the diffraction angle range 2θ = ≈5°–80° with Cu Ka radiation (λ = 1.5418 Å) at 40 kV, 40 mA. X-ray photoelectron spectroscopy (XPS) was measured on a Perkin–Elmer model PHI 5500 XPS system with a resolution of 0.3–0.5 eV from a monochromated aluminum anode X-ray source with Mo Kα radiation (1486.6 eV). All the XPS spectra were calibrated using the C 1s peak of carbon present at 284.80 eV. Field-emission scanning electron microscopy (FESEM) was characterized by a Nona-Nano SEM450 operated at an accelerating voltage of 5 kV. Transmission electron microscopy (TEM), high-resolution TEM (HRTEM), high-angle annular dark-field scanning TEM (HAADF STEM), and energy dispersive X-ray spectroscopy (EDX) were performed on Tecnai G2 TF30 operated at 300 kV. FT-IR spectra (KBr pellets) were obtained on a Thermo Electron NEXUS 670 FT-IR spectrometer. The contents of Fe, Co, Ni, Mn, and Cr were measured by inductively coupled plasma emission spectroscopy (ICP-OES) conducted on a PE Avio 200 instrument. ICP mass spectrometry (ICP-MS) was measured on an iCAP Qc spectrometer at 1150 W. The Raman spectra were recorded using a LabRAM HR Evolution Raman spectrometer (HORIBA) with a 532 nm laser wavelength.

The mixed configuration entropy of HEAs could be depicted by the following equation

$$\Delta S_{mix} = -R \sum_{i=1}^{n} x_i \ln x_i \quad (1)$$

where R was the molar gas constant, and x_i represented the mole fraction of the elemental component.[15]

Electrochemical Measurements: Electrocatalytic activity measurements of the as-synthesized samples were performed with a CHI760E electrochemistry workstation (CH Instruments, Inc.) using a standard three-electrode electrochemical cell with Pt sheet and Hg/HgO as the counter and reference electrode, respectively. Chronopotentiometry (CP) responses curve was performed at a high constant current density of 100 mA cm^{-2} in 1 M KOH using a carbon rod as counter electrode at room temperature. Long-term stability measurements under industrial conditions were performed in a Teflon container at 500 mA cm^{-2} in 6.0 M KOH using a carbon rod as the counter electrode at 85 °C. ECSAs were calculated by dividing C_{dl} by a specific capacitance (C_s, assumed as 0.04 mF cm^{-2} in 1 M KOH). Based on the LSV, turnover frequency (TOF) of the catalysts could be calculated by TOF = $j \times A$ / (4×F×m/M), where j was the current density (mA cm^{-2}) at a given overpotential, A was surface area of working electrode, F was the faraday constant (96 485 C mol^{-1}), m was mass loading of the catalyst, and M was the molecular weight of the catalyst unified with one active center per formula unit. All the catalytically related metal atoms were assumed to be accessible during the OER catalysis.

DFT Calculations: DFT calculations were conducted by using the CASTEP package to investigate the electronic modulation induced by the HEO and its influences on the OER process.[27] To guarantee an accurate description of the exchange-correlation energy, the generalized gradient approximation (GGA) in the scheme of Perdew–Burke–Ernzerhof (PBE) was applied.[28] For all geometry optimizations, the cutoff energy was set to 380 eV based on the ultrasoft pseudopotential scheme. In addition, the Broyden–Fletcher–Goldfarb–Shannon (BFGS) algorithm and the *k*-point mesh with coarse quality was also chosen. The HEO model was established based on the experimental data of $NiMnCrO_4$. The following convergence criteria for geometry optimization were adopted: the Hellmann–Feynman forces not exceeding 0.001 eV $Å^{-1}$, the total energy of less than 5×10^{-5} eV $atom^{-1}$, and the inter-ionic displacement of smaller than 0.005 Å.

Supporting Information

Supporting Information is available from the Wiley Online Library or from the author.

Acknowledgements

This work was supported by the National Natural Science Foundation of China (Grant Nos: 52364041, 51974141, and 51864024), the National Natural Science Foundation of China/RGC Joint Research Scheme (Grant No. N_PolyU502/21), the funding for Projects of Strategic Importance of The Hong Kong Polytechnic University (Project Code: 1-ZE2V), Shenzhen Fundamental Research Scheme-General Program (Grant No. JCYJ20220531090807017), the Natural Science Foundation of Guangdong Province (No. 2023A1515012219) and Departmental General Research Fund (Project Code: ZVUL) from The Hong Kong Polytechnic University. B.H. also thanks the support from Research Centre for Carbon-Strategic Catalysis (RC-CSC), Research Institute for Smart Energy (RISE), and Research Institute for Intelligent Wearable Systems (RI-IWEAR) of the Hong Kong Polytechnic University. T.G. and Z.W. acknowledged the European Research Executive Agency (Project No. 101079184-FUNLAYERS).

Conflict of Interest

The authors declare no competing interests.

Author Contributions

J.H., T.G., and X.Z. contributed equally to this work. J.H., C.Z., and L.Z. developed the idea and designed the experiments. Y.M. synthesized the

catalyst and performed electrochemical experiments. J.H., T.G., Y.M., Y.W., and L.M. characterized the morphology and chemical structure of the catalysts. M.S. and B.H. performed theoretical calculations. X.Z. and J.L. carried out the XAS measurements and analyses. J.H., Y.M., C.Z., B.H., Y.F., and Z.W. wrote and revised the manuscript. B.H., L.Z. and Z.W. supervised the project. All authors discussed the results and directed the entire study.

Data Availability Statement

The data that support the findings of this study are available from the corresponding author upon reasonable request.

Keywords

heterostructures, high-entropy alloys, high-entropy oxides, long-term stability, oxygen evolution reaction

Received: October 19, 2023
Revised: December 28, 2023
Published online:

[1] a) J. Wang, Y. Gao, H. Kong, J. Kim, S. Choi, F. Ciucci, Y. Hao, S. Yang, Z. Shao, J. Lim, *Chem. Soc. Rev.* **2020**, *49*, 9154; b) J. Hu, C. Zhang, L. Jiang, H. Lin, Y. An, D. Zhou, M. K. H. Leung, S. Yang, *Joule* **2017**, *1*, 383.

[2] a) C. Hu, L. Zhang, J. Gong, *Energy Environ. Sci.* **2019**, *12*, 2620; b) K. Zhang, R. Zou, *Small* **2021**, *17*, 2100129; c) C. Zhang, Q. Qi, Y. Mei, J. Hu, M. Sun, Y. Zhang, B. Huang, L. Zhang, S. Yang, *Adv. Mater.* **2023**, *35*, 2208904.

[3] a) X. Zhang, M. Jin, F. Jia, J. Huang, A. Amini, S. Song, H. Yi, C. Cheng, *Energy Environ. Mater.* **2023**, *1*, e12457; b) F. Zeng, C. Mebrahtu, L. Liao, A. K. Beine, R. Palkovits, *J. Energy Chem.* **2022**, *69*, 301.

[4] a) S. Wang, W. Huo, F. Fang, Z. Xie, J. K. Shang, J. Jiang, *Chem. Eng. J.* **2022**, *429*, 132410; b) P. Li, X. Wan, J. Su, W. Liu, Y. Guo, H. Yin, D. Wang, *ACS Catal.* **2022**, *12*, 11667.

[5] a) Y. Ma, Y. Ma, Q. Wang, S. Schweidler, M. Botros, T. Fu, H. Hahn, T. Brezesinski, B. Breitung, *Energy Environ. Sci.* **2021**, *14*, 2883; b) B. Jiang, Y. Yu, J. Cui, X. Liu, L. Xie, J. Liao, Q. Zhang, Y. Huang, S. Ning, B. Jia, B. Zhu, S. Bai, L. Chen, S. J. Pennycook, J. He, *Science* **2021**, *371*, 830.

[6] S. Wang, B. Xu, W. Huo, H. Feng, X. Zhou, F. Fang, Z. Xie, J. K. Shang, J. Jiang, *Appl Catal., B* **2022**, *313*, 121472.

[7] H. Liu, H. Qin, J. Kang, L. Ma, G. Chen, Q. Huang, Z. Zhang, E. Liu, H. Lu, J. Li, N. Zhao, *Chem. Eng. J.* **2022**, *435*, 134898.

[8] Y. Mei, Y. Feng, C. Zhang, Y. Zhang, Q. Qi, J. Hu, *ACS Catal.* **2022**, *12*, 10808.

[9] B. Song, Y. Yang, M. Rabbani, T. T. Yang, K. He, X. Hu, Y. Yuan, P. Ghildiyal, V. P. Dravid, M. R. Zachariah, W. A. Saidi, Y. Liu, R. Shahbazian-Yassar, *ACS Nano* **2020**, *14*, 15131.

[10] H. Li, J. Lai, Z. Li, L. Wang, *Adv. Funct. Mater.* **2021**, *31*, 2106715.

[11] Z. Jin, J. Lyu, Y.-L. Zhao, H. Li, Z. Chen, X. Lin, G. Xie, X. Liu, J.-J. Kai, H.-J. Qiu, *Chem. Mater.* **2021**, *33*, 1771.

[12] J. Hu, L. Wu, K. A. Kuttiyiel, K. R. Goodman, C. Zhang, Y. Zhu, M. B. Vukmirovic, M. G. White, K. Sasaki, R. R. Adzic, *J. Am. Chem. Soc.* **2016**, *138*, 9294.

[13] Y. Yao, Q. Dong, A. Brozena, J. Luo, J. Miao, M. Chi, C. Wang, I. G. Kevrekidis, Z. J. Ren, J. Greeley, G. Wang, A. Anapolsky, L. Hu, *Science* **2022**, *376*, eabn3103.

[14] a) D. Wang, Z. Liu, S. Du, Y. Zhang, H. Li, Z. Xiao, W. Chen, R. Chen, Y. Wang, Y. Zou, S. Wang, *J. Mater. Chem. A* **2019**, *7*, 24211; b) F. Shahbazi Farahani, B. Mecheri, M. R. Majidi, E. Placidi, A. D'epifanio, *Carbon* **2019**, *145*, 716.

[15] Y. Xin, S. Li, Y. Qian, W. Zhu, H. Yuan, P. Jiang, R. Guo, L. Wang, *ACS Catal.* **2020**, *10*, 11280.

[16] Q. Qi, J. Hu, S. Guo, H. Song, S. Wang, Y. Yao, T. Le, W. Li, C. Zhang, L. Zhang, *Appl. Catal., B* **2021**, *299*, 120637.

[17] a) X. Chang, M. Zeng, K. Liu, L. Fu, *Adv. Mater.* **2020**, *32*, 1907226; b) Z. Jin, J. Lv, H. Jia, W. Liu, H. Li, Z. Chen, X. Lin, G. Xie, X. Liu, S. Sun, H.-J. Qiu, *Small* **2019**, *15*, e1904180; c) F. Mckay, Y. Fang, O. Kizilkaya, P. Singh, D. D. Johnson, A. Roy, D. P. Young, P. T. Sprunger, J. C. Flake, W. A. Shelton, Y. Xu, *J. Phys. Chem. C* **2021**, *125*, 17008.

[18] Z.-J. Chen, T. Zhang, X.-Y. Gao, Y.-J. Huang, X.-H. Qin, Y.-F. Wang, K. Zhao, X. Peng, C. Zhang, L. Liu, M.-H. Zeng, H.-B. Yu, *Adv. Mater.* **2021**, *33*, 2101845.

[19] Y. Zhou, S. Sun, C. Wei, Y. Sun, P. Xi, Z. Feng, Z. J. Xu, *Adv. Mater.* **2019**, *31*, 1902509.

[20] a) L. Bai, C.-S. Hsu, D. T. L. Alexander, H. M. Chen, X. Hu, *Nat. Energy* **2021**, *6*, 1054; b) Y. Luo, Z. Zhang, F. Yang, J. Li, Z. Liu, W. Ren, S. Zhang, B. Liu, *Energy Environ. Sci.* **2021**, *14*, 4610.

[21] Q. Feng, S. Zhao, Y. Wang, J. Dong, W. Chen, D. He, D. Wang, J. Yang, Y. Zhu, H. Zhu, L. Gu, Z. Li, Y. Liu, R. Yu, J. Li, Y. Li, *J. Am. Chem. Soc.* **2017**, *139*, 7294.

[22] S. Zhou, Y. Zhao, R. Shi, Y. Wang, A. Ashok, F. Héraly, T. Zhang, J. Yuan, *Adv. Mater.* **2022**, *34*, 2204388.

[23] J. N. Tiwari, N. K. Dang, S. Sultan, P. Thangavel, H. Y. Jeong, K. S. Kim, *Nat. Sustain.* **2020**, *3*, 556.

[24] A. Nairan, P. Zou, C. Liang, J. Liu, D. Wu, P. Liu, C. Yang, *Adv. Funct. Mater.* **2019**, *29*, 1903747.

[25] a) L. Sharma, N. K. Katiyar, A. Parui, R. Das, R. Kumar, C. S. Tiwary, A. K. Singh, A. Halder, K. Biswas, *Nano Res.* **2022**, *15*, 4799; b) W. Dai, T. Lu, Y. Pan, *J. Power Sources* **2019**, *430*, 104; c) X. Zhao, Z. Xue, W. Chen, Y. Wang, T. Mu, *ChemSusChem* **2020**, *13*, 2038; d) J. Tang, J. L. Xu, Z. G. Ye, X. B. Li, J. M. Luo, *J. Mater. Sci. Technol.* **2021**, *79*, 171; e) J. X. Yang, B.-H. Dai, C.-Y. Chiang, I.-C. Chiu, C.-W. Pao, S.-Y. Lu, I.-Y. Tsao, S.-T. Lin, C.-T. Chiu, J.-W. Yeh, P.-C. Chang, W.-H. Hung, *ACS Nano* **2021**, *15*, 12324; f) Z. Ding, J. Bian, S. Shuang, X. Liu, Y. Hu, C. Sun, Y. Yang, *Adv. Sustain. Syst.* **2020**, *4*, 1900105; g) F. Liu, M. Yu, X. Chen, J. Li, H. Liu, F. Cheng, *Chin. J. Catal.* **2022**, *43*, 122; h) X. Zhao, Z. Xue, W. Chen, X. Bai, R. Shi, T. Mu, *J. Mater. Chem. A* **2019**, *7*, 26238; i) H.-J. Qiu, G. Fang, J. Gao, Y. Wen, J. Lv, H. Li, G. Xie, X. Liu, S. Sun, *ACS Mater. Lett.* **2019**, *1*, 526; j) L.-H. Liu, N. Li, M. Han, J.-R. Han, H.-Y. Liang, *Rare Met.* **2022**, *41*, 125; k) H. Wang, R. Wei, X. Li, X. Ma, X. Hao, G. Guan, *J. Mater. Sci. Technol.* **2021**, *68*, 191; l) S. Q. Zhao, H. Y. Wu, R. Yin, X. N. Wang, H. Z. Zhong, Q. Fu, W. J. Wan, T. Cheng, Y. Shi, G. X. Cai, C. Z. Jiang, F. Ren, *J. Alloys Compd.* **2021**, *868*, 159108; m) P. Ma, S. Zhang, M. Zhang, J. Gu, L. Zhang, Y. Sun, W. Ji, Z. Fu, *Sci. China Mater.* **2020**, *63*, 2613; n) K. Gu, X. Zhu, D. Wang, N. Zhang, G. Huang, W. Li, P. Long, J. Tian, Y. Zou, Y. Wang, R. Chen, S. Wang, *J. Energy Chem.* **2021**, *60*, 121; o) K. Huang, B. Zhang, J. Wu, T. Zhang, D. Peng, X. Cao, Z. Zhang, Z. Li, Y. Huang, *J. Mater. Chem. A* **2020**, *8*, 11938; p) Z. Chen, J. Wen, C. Wang, X. Kang, *Small* **2022**, *4255*, 2204255; q) S. Xu, X. Yu, L. Luo, W. Li, Y. Du, Q. Kong, Q. Wu, *Nano Res.* **2022**, *15*, 4942; r) W. Li, Y. Deng, L. Luo, Y. Du, X. Cheng, Q. Wu, *J. Colloid Interface Sci.* **2023**, *639*, 416; s) W. Dai, X. Yang, F. Hu, W. Cao, C. Zhao, Y. Zhang, S. Huang, *J. Alloys Compd.* **2023**, *952*, 169987; t) W. Cao, X. Yang, W. Dai, B. Wu, Y. Zhang, C. Zhao, Y. Sui, S. Huang, *New J. Chem.* **2023**, *47*, 12670.

[26] H. B. Tao, Y. Xu, X. Huang, J. Chen, L. Pei, J. Zhang, J. G. Chen, B. Liu, *Joule* **2019**, *3*, 1498.

[27] S. J. Clark, M. D. Segall, C. J. Pickard, P. J. Hasnip, M. J. Probert, K. Refson, M. C. Payne, *Z. Kristallogr.* **2005**, *220*, 567.

[28] a) J. P. Perdew, K. Burke, M. Ernzerhof, *Phys. Rev. Lett.* **1996**, *77*, 3865; b) P. J. Hasnip, C. J. Pickard, *Comput. Phys. Commun.* **2006**, *174*, 24; c) J. P. Perdew, J. A. Chevary, S. H. Vosko, K. A. Jackson, M. R. Pederson, D. J. Singh, C. Fiolhais, *Phys. Rev. B* **1992**, *46*, 6671.